

Hybrid Barium Titanate Waveguide Designs For Efficient Nonlinear Frequency Conversion

Trevor G. Vrckovnik^{1,2,3}, Dennis Arslan¹, Falk Eilenberger^{1,2,3}, and Sebastian W. Schmitt^{1,2,*}

¹Fraunhofer Institute for Applied Optics and Precision Engineering IOF, Albert-Einstein-Str. 7, 07745 Jena, Germany

²Institute of Applied Physics, Abbe Center of Photonics, Friedrich Schiller University Jena, Albert-Einstein-Str. 15, 07745 Jena, Germany

³Max Planck School of Photonics, Albert-Einstein-Str. 15, 07745 Jena, Germany

*E-mail: sebastian.wolfgang.schmitt@iof.fraunhofer.de

Barium titanate (BaTiO₃) is emerging as a powerful integrated photonic material, combining strong $\chi^{(2)}$ and electro-optic nonlinearities with rapidly improving thin-film waveguide quality. Recent demonstrations of low-loss BaTiO₃ waveguides and high-Q resonators have established BaTiO₃-on-insulator as a promising platform for next-generation frequency-conversion and quantum photonic technologies. However, while BaTiO₃ electro-optic modulators are now well developed, nonlinear BaTiO₃ waveguide engineering remains comparatively immature. Techniques widely used in lithium niobate, such as periodic poling for quasi-phase-matching, are poorly suited to BaTiO₃ because epitaxial thin films exhibit high coercive fields, strong strain-clamping effects, multivariant domain structures, and slow, complex switching dynamics. These factors make accurate periodic poling challenging and hinder the development of efficient $\chi^{(2)}$ frequency converters. Here, we introduce a fabrication-robust alternative based on linear-nonlinear hybrid waveguides, where TiO₂ is selectively incorporated into BaTiO₃ ridge waveguides to enhance nonlinear mode overlap while relying solely on modal phase-matching. Using coupled-mode-theory simulations, we identify phase-matched geometries and show that the hybrid design achieves a 2.75x increase in normalized second harmonic generation efficiency over monolithic BaTiO₃ waveguides. The uniform, lithographically defined cross-section makes the approach highly scalable. These results position hybrid BaTiO₃-TiO₂ waveguides as a practical route to CMOS-compatible, high-efficiency $\chi^{(2)}$ devices for integrated quantum photonics.

1 Introduction

Thin-film ferroelectric oxides have recently attracted substantial interest for integrated photonics because they combine strong nonlinear and electro-optic properties with compatibility to semiconductor fabrication workflows^[1-3]. Among these materials, barium titanate (BaTiO₃) stands out due to its large Pockels coefficient, high second-order nonlinear susceptibility ($\chi^{(2)}$), and ability to form epitaxial layers on silicon-based substrates^[4]. Recently, advances in thin-film growth, planarization, and patterning have enabled low-loss BaTiO₃ waveguides and high-Q resonators from BaTiO₃-on-insulator platforms^[5-7].

The strong electro-optic effect of BaTiO₃ has enabled compact modulators with low drive voltages and multi-GHz bandwidths^[8-11], and non-volatile phase shifters^[9]. The same large $\chi^{(2)}$ nonlinearity suggests strong potential for frequency conversion and photon-pair generation processes such as second harmonic generation (SHG). However, in contrast to lithium niobate (LiNbO₃) where quasi-phase-matching via periodic poling underpins a large ecosystem of nonlinear devices^[12-14], it remains questionable whether BaTiO₃ thin films support reliable and scalable domain inversion engineering. Strong substrate-induced clamping stabilizes multivariant, strain-dependent domain configurations and coercive fields, while the reduced remnant polarization of BaTiO₃ thin films promotes relaxation and back-switching, together limiting controlled and repeatable 180° domain switching^[15-20].

Consequently, stable periodic poling in BaTiO₃ is highly sensitive to substrate-specific strain and boundary conditions and requires narrow, carefully engineered growth windows. Although electric field induced periodic domain inversion has recently been demonstrated on dysprosium scandate (DyScO₃) substrates with strontium ruthenate (SrRuO₃) electrodes^[21], this remains a substrate-specific result of limited photonic relevance due to DyScO₃'s high refractive index that does not allow mode confinement in the BaTiO₃ layer and losses in the SrRuO₃ electrode. Moreover, periodic poling can introduce additional domain walls and defects, increasing

optical scattering losses in BaTiO₃ waveguides^[22].

These constraints motivate alternative $\chi^{(2)}$ frequency conversion strategies, notably modal phase-matching, which avoids micro- or nanoscale periodic poling and ferroelectric domain engineering. In this strategy, the waveguide dimensions are chosen such that the effective refractive index of the pump mode at the fundamental frequency, typically the fundamental transverse electric (TE) or transverse magnetic (TM) mode, is equal to the effective refractive index of a second harmonic mode, typically a higher order mode. This results in waveguides which are generally simpler from a fabrication point of view, but which typically have lower efficiencies due to the mode order mismatch causing smaller mode overlaps. To combat this, the cross-section of the waveguides can be modified to help maximize the mode overlap. Comparable approaches have been shown in LiNbO₃ using double layered waveguides^[23-25], hybrid linear-nonlinear waveguides^[26-28], or the introduction of asymmetries to the cross-section^[29]. However, to date designs for maximizing the efficiency of frequency conversion processes with BaTiO₃ are missing. In this work, we propose hybrid BaTiO₃-TiO₂ waveguides, in which a thin TiO₂ layer modifies modal confinement and significantly enhances nonlinear overlap^[30,31]. Because this strategy relies solely on lithographic definition of the waveguide geometry, it is inherently scalable and avoids the limitations of domain inversion in BaTiO₃.

The following sections develop a coupled-mode-theory design framework for these hybrid structures, quantify the achievable second-harmonic-generation efficiency, and benchmark their performance against both monolithic BaTiO₃ waveguides and established nonlinear photonic platforms. Our results show that these hybrid BaTiO₃-TiO₂ waveguides provide a practical and CMOS-compatible pathway toward efficient $\chi^{(2)}$ devices on the emerging BaTiO₃ photonic platform.

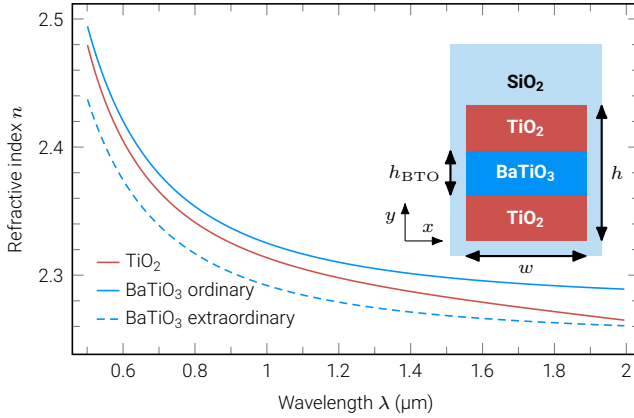


Fig. 1 | Refractive indices of the two BaTiO_3 axes compared with TiO_2 . The inset shows the cross-section of the hybrid waveguide geometries discussed in this paper.

2 Working Principle of Hybrid BaTiO_3 Waveguides

The mode overlap between a fundamental frequency and second harmonic eigenmode in a waveguide can be calculated as^[32],

$$\kappa_m = \left\| \frac{2\omega\epsilon_0}{4} \iint \overline{\mathbf{E}_m(x, y, 2\omega)} \cdot \mathbf{P}_{\text{NL}}(x, y, 2\omega) \, dx \, dy \right\| \quad (1)$$

$$P_{\text{NL},i}(x, y, 2\omega) = \sum_{jk} \frac{1}{2} \chi_{ijk}^{(2)}(x, y) E_j(x, y, \omega) E_k(x, y, \omega) \quad (2)$$

where κ_m is the mode overlap, $\mathbf{E}_m(2\omega)$ is the normalized electric field of the second harmonic eigenmode of interest, and $\mathbf{E}(\omega)$ is the normalized electric field of the fundamental frequency input eigenmode. The units of κ_m are $\frac{\sqrt{W}}{m}$, and therefore it represents how much energy is converted into the second harmonic mode per unit time and unit of propagation length, without considering potential phase-matching problems.

We note that in calculating the mode overlap, the fundamental frequency mode gives rise to the nonlinear polarization density field (mediated by $\chi^{(2)}$), which in turn is projected on to the second harmonic mode and then integrated across the full waveguide cross-section. The second harmonic modes which are naturally phase-matched in monolithic cuboid waveguides tend to be higher order modes, meaning the electric fields have multiple lobes in the transverse plane, with alternating signs. This means that the integral across the full plane has both positive and negative contributions, leading to a smaller mode overlap. Hybrid waveguides can help solve this problem by selectively placing linear (centrosymmetric such that $\chi^{(2)} = 0$) materials in the waveguide cross-section, so that the nonlinear interaction only takes place within lobes of a single sign.

3 $\text{TiO}_2\text{-}\text{BaTiO}_3\text{-}\text{TiO}_2$ Platform Concept

Fig. 1 shows how two established waveguide materials, BaTiO_3 and TiO_2 , can be combined for a hybrid waveguide design. TiO_2 would be a good candidate as the linear material to combine with BaTiO_3 for hybrid waveguides, as its refractive index has a value between the ordinary and extraordinary refractive indices of BaTiO_3 . This means that the modes supported by a hybrid waveguide core would be very similar

to those for a monolithic BaTiO_3 core, since the mode profiles and effective refractive index only depend on the linear susceptibility.

We propose to realize a $\text{TiO}_2\text{-}\text{BaTiO}_3\text{-}\text{TiO}_2$ multilayer stack using a layer-by-layer growth and bonding sequence that adds only minimal complexity to established oxide photonics fabrication workflows. In a first step, individual oxide layers are deposited and optimized separately: crystalline BaTiO_3 thin films are grown on a suitable growth substrate under conditions tailored for ferroelectric and nonlinear performance^[19,33,34] or fabricated using crystal ion slicing and subsequent annealing^[35-37], while TiO_2 layers are deposited independently using standard oxide thin-film techniques such as sputtering or atomic layer deposition, which are fully compatible with photonic device fabrication and known to yield low-loss waveguides with strong optical confinement^[38-41].

Subsequently, the TiO_2 and BaTiO_3 layers are combined via direct wafer bonding, exploiting the demonstrated compatibility of BaTiO_3 with metal-oxide layers such as TiO_2 and Al_2O_3 ^[42,43]. This bonding step enables the formation of a vertically symmetric $\text{TiO}_2\text{-}\text{BaTiO}_3\text{-}\text{TiO}_2$ stack, after which the original growth substrates can be removed if required. In a final step, standard lithography and dry-etching processes are applied to pattern the bonded stack into photonic structures such as waveguides or resonators. This decoupled growth-bonding-patterning sequence relaxes constraints imposed by direct epitaxial growth on photonic substrates, mitigates issues related to lattice mismatch and strain engineering, and provides a scalable and flexible route toward integrated BaTiO_3 -based electro-optic and nonlinear photonic devices.

4 Geometry Optimization

To design the hybrid waveguides, we first simulate monolithic BaTiO_3 waveguides to find geometries that naturally have good modal phase-matching with a second harmonic mode. The profile of this well phase-matched second harmonic mode can then be analyzed to see where the linear material (TiO_2) should be placed to maximize the mode overlap. Then, simulations of this hybrid design can be performed to optimize the layer thicknesses and geometry, given the slight differences to the eigenmodes induced by the inclusion of the linear material.

Fig. 2a shows simulation results of a monolithic BaTiO_3 cuboid waveguide of varying widths and heights, encased in SiO_2 . A coupled mode theory (CMT) based solving tool was used to simulate SHG in each waveguide, as this allows us to view exactly which eigenmodes are used in the interactions and where the energy is concentrated in the waveguide. For each waveguide geometry, the TM_{00} mode at the fundamental wavelength (1550 nm) was given an initial amplitude of $1 \sqrt{W}$, and all other mode amplitudes were set to 0. After a propagation distance of 100 μm , the normalized SHG efficiency of the waveguide was recorded.

Bands of efficient waveguides appear in the sweep, due to a particular second harmonic mode being well phase-matched to the input mode. The CMT simulation allows us to view the profile of these modes, and then selectively place a linear material to help improve the mode overlap, and thus SHG efficiency. For example, from Fig. 2a the most efficient waveguide was when the BaTiO_3 core had a height of 0.78 μm and a width of 0.56 μm (as indicated by the cyan square). In this case, the phase-matched second harmonic mode carrying the

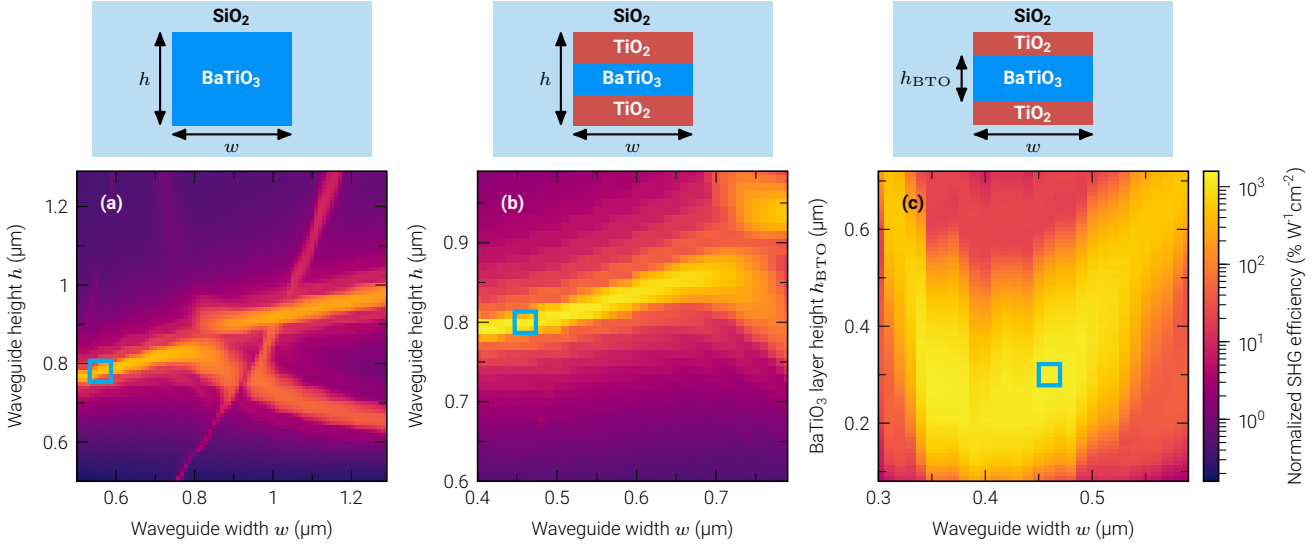


Fig. 2 | Geometry optimization sweeps of the hybrid waveguides. **(a)** Monolithic BaTiO_3 waveguide cores showing bands of high efficiency where there are naturally second harmonic modes phase-matched to the TM_{00} mode at the fundamental frequency. **(b)** Hybrid waveguides with varying total heights and widths, but all three layers kept equal. **(c)** Hybrid waveguides with the total core height fixed at 0.8 μm but varying widths and height of the BaTiO_3 layer. The cyan square in each plot represents the waveguide with the largest normalized SHG efficiency. Above each plot is the corresponding waveguide cross-section with the two varying geometric parameters indicated.

energy is the TE_{02} mode, which has three main lobes stacked vertically in its electric field. A hybrid waveguide can then be composed by having sections of TiO_2 covering the top and bottom lobes, and BaTiO_3 in the central lobe. The BaTiO_3 layer is placed in the middle as this is where the input mode is concentrated.

Fig. 2b shows how the hybrid waveguide geometry was then optimized, first by keeping the height of all three layers equal but changing the total height and width of the waveguide. The bands of efficient structures follow a very similar shape as those from the monolithic BaTiO_3 waveguides, proving that the addition of the TiO_2 layers has little effect on the phase-matching. The ideal height for the total waveguide structure was found to be 0.8 μm . Then, in Fig. 2c the geometry was further optimized by keeping the total waveguide height fixed, but varying the height of the BaTiO_3 layer along with the width of the waveguide. The optimized hybrid waveguide was found to have a width of 0.46 μm , with a BaTiO_3 layer 0.30 μm high sandwiched between two layers of TiO_2 each 0.25 μm high.

The bands of high efficiency in Fig. 2b have a manufacturing tolerance of 30-40 nm, while in Fig. 2c the manufacturing tolerance of the BaTiO_3 layer height is ~ 200 nm. This makes sense as these bands are determined by the phase-matching of a second harmonic mode with the input mode. Since TiO_2 has a refractive index very close to BaTiO_3 , the total structure height and width have a bigger impact on the effective refractive indices of the eigenmodes compared to the height of the individual layers in the core. This is advantageous from a manufacturing perspective, as it does not impose stringent thickness tolerances on the BaTiO_3 film itself. Instead, once the BaTiO_3 layer has been fabricated and its thickness measured, the TiO_2 cladding layers can be deposited accordingly to achieve a total stack height of 0.80 μm .

Fig. 3 shows how the hybrid waveguides improve the mode overlap in the waveguide. The integral across the BaTiO_3 cross-section in the monolithic waveguides includes components from both signs in the second harmonic mode (Fig. 3c).

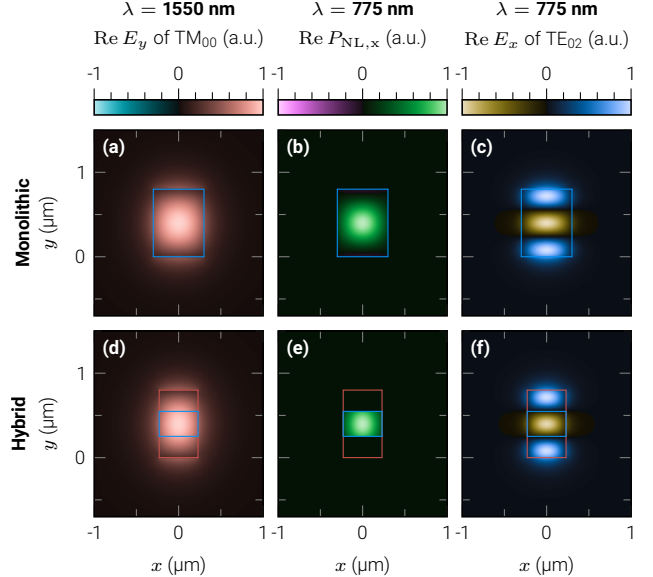


Fig. 3 | Dominant components of the **(a,d)** fundamental electric, **(b,e)** nonlinear polarization density, and **(c,f)** second harmonic electric fields for **(a-c)** monolithic and **(d-f)** hybrid waveguide cores. The regions filled with BaTiO_3 and TiO_2 are outlined by blue and red lines, respectively. The remaining regions extending to the edges of each plot are filled with SiO_2 .

In comparison, Fig. 3f shows how the hybrid structure isolates each lobe of the eigenmode to a specific layer in the waveguide core, and therefore the integral over the BaTiO_3 layer only includes a single sign. The result is that the mode overlap of the hybrid waveguide is 1.6 times larger, despite having a cross-sectional area with only 0.28 times as much BaTiO_3 compared to the monolithic waveguide.

This increased mode overlap also results in an increased SHG efficiency, as seen in Fig. 4 plotted over a propagation distance of 100 μm . The normalized SHG efficiency of the monolithic waveguide is $510.5 \text{ \%} \cdot \text{W}^{-1} \cdot \text{cm}^{-2}$, while for the hybrid structure it is $1404.5 \text{ \%} \cdot \text{W}^{-1} \cdot \text{cm}^{-2}$. This efficiency is significantly larger than theoretical efficiencies predicted for

other material platforms such as monolithic GaP waveguides ($6.1\% \cdot W^{-1} \cdot cm^{-2}$ ^[44]), or AlN-SiN hybrid waveguides ($12\% \cdot W^{-1} \cdot cm^{-2}$ ^[27]). As well, these designs show that BaTiO₃ waveguides can have theoretical efficiencies of the same order of magnitude seen in hybrid LiNbO₃ waveguides ($2900\% \cdot W^{-1} \cdot cm^{-2}$ ^[26]), periodically poled LiNbO₃ waveguides ($3000\% \cdot W^{-1} \cdot cm^{-2}$ ^[12]) and in particular periodically poled thin-film LiNbO₃ waveguides ($1600\% \cdot W^{-1} \cdot cm^{-2}$ ^[45]), which is the standard implementation for LiNbO₃-based integrated optics. It is also worth noting that because our hybrid waveguide platform uses modal phase-matching and therefore has an unchanging cross-section, these devices should be easier to fabricate compared to designs relying on periodic poling, leading to them being more reproducible, scalable, and capable of broadband operation.

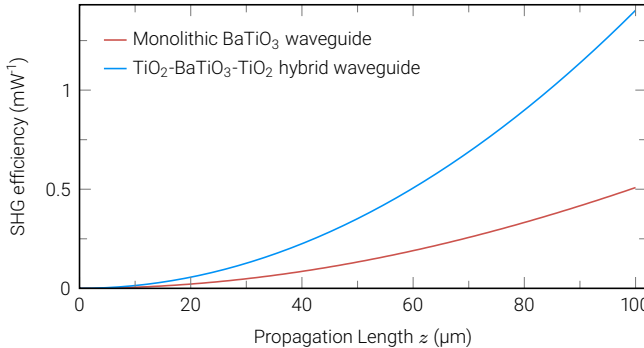


Fig. 4 | Comparison of SHG efficiency between the monolithic BaTiO₃ waveguide and the hybrid waveguide over a 100 μm long propagation distance.

5 Conclusion

In this work, we proposed a new platform and design scheme to increase the efficiency of nonlinear frequency conversion processes in BaTiO₃ waveguides. This was done by first using modal phase-matching to find geometries which naturally have high efficiencies without the need for periodic poling. By knowing the profile of the phase-matched modes, the nonlinear efficiency could be further enhanced by creating a linear-nonlinear hybrid structure, and selectively placing the nonlinear material in the waveguide cross-section.

We propose that this is best done by having a TiO₂ layer both above and below the BaTiO₃ layer, as these materials have similar linear refractive indices, and thus the phase-matching requirements are similar to a monolithic BaTiO₃ waveguide. Through optimization of the hybrid waveguide geometries, the normalized SHG efficiency was found to be 2.75 times larger than optimized monolithic BaTiO₃ waveguides, and of the same order of magnitude as various waveguide designs from LiNbO₃. Overall, these hybrid waveguides offer the ability to introduce efficient and easily scalable nonlinear frequency conversion applications to the already established electro-optic modulation BaTiO₃ platform, opening the door to new possibilities for nonlinear and quantum photonic integrated circuits.

Methods

Simulation Methods

From Maxwell's curl equations the vector wave equation can be derived, the solutions of which are a series of eigenvectors

with corresponding eigenvalues. Each eigenvector describes how an electric and magnetic field can propagate in the waveguide, and the corresponding eigenvalue is known as the propagation constant. The combined electric and magnetic field is known as an eigenmode, and once normalized, eigenmodes of a specific frequency have the unique property that they are all orthonormal to each other. Therefore, any electromagnetic field propagating through a waveguide can be decomposed into a linear superposition of eigenmodes as

$$\mathbf{E}(x, y, z, \omega) = \sum_m A_m(z) \mathbf{E}_m(x, y, \omega) e^{i\beta_m z} \quad (3)$$

$$\mathbf{H}(x, y, z, \omega) = \sum_m A_m(z) \mathbf{H}_m(x, y, \omega) e^{i\beta_m z} \quad (4)$$

where A_m is the amplitude of the eigenmode, \mathbf{E}_m and \mathbf{H}_m are the electric and magnetic mode profiles in the transverse plane, β_m is the propagation constant of the mode, and z is the current position in the propagation direction.

Using Eq. (3) as an ansatz in the vector wave equation, we find a set of coupled differential equations that describe how each mode amplitude evolves as the mode propagates along the waveguide^[32]:

$$\frac{\partial}{\partial z} A_m(z) = i \frac{\omega}{4} \epsilon_0 e^{-i\beta_m z} \int_{\mathbb{R}^2} \overline{\mathbf{E}_m(x, y, \omega)} \cdot \mathbf{P}_{NL}(x, y, z, \omega) dx dy \quad (5)$$

We then find the eigenmodes of a specific waveguide geometry and numerically solve the corresponding set of coupled differential equations from Eq. (5) as an initial value problem. This results in a list of complex mode amplitudes, each evaluated at each z -step of the initial value solver. With these amplitudes, the total \mathbf{E} and \mathbf{H} fields at each frequency can be found in the waveguide using Eqs. (3),(4).

If we assume that the electric field consists of only harmonic waves at the fundamental (ω) and second harmonic (2ω) frequencies, it can be expressed as,

$$\mathbf{E}(t) = \text{Re}(\mathbf{E}(\mathbf{r}, \omega) e^{-i\omega t} + \mathbf{E}(\mathbf{r}, 2\omega) e^{-i2\omega t}) \quad (6)$$

and the total guided power $P(z)$ at a point z in the waveguide can be decomposed into the contributions of the modes as

$$P(z) = P(z, \omega) + P(z, 2\omega) \quad (7)$$

$$P(z, q) = \frac{1}{2} \int_{\mathbb{R}^2} \text{Re}(\mathbf{E}(\mathbf{r}, \omega) \times \overline{\mathbf{H}(\mathbf{r}, \omega)}) \cdot \hat{\mathbf{z}} dx dy \quad (8)$$

$$+ \frac{1}{2} \int_{\mathbb{R}^2} \text{Re}(\mathbf{E}(\mathbf{r}, 2\omega) \times \overline{\mathbf{H}(\mathbf{r}, 2\omega)}) \cdot \hat{\mathbf{z}} dx dy$$

Without loss of generality, it can be assumed that the waveguide starts at $z = 0$ and is excited there with a certain power at the fundamental frequency $P(0, \omega)$. The normalized efficiency η with which second harmonic photons are generated is then defined as

$$\eta(z) := \frac{P(z, 2\omega)}{P(0, \omega)^2} \quad (9)$$

with units of $[\eta] = W^{-1}$. Since $P(z, 2\omega)$ is generally proportional to $P(0, \omega)^2 z^2$, i.e. dependent on the square of the waveguide length, we can further define a normalized efficiency $\tilde{\eta}$

$$\tilde{\eta} := \arg \min_a \int_0^{\ell} [\eta(z) - az^2]^2 dz = \frac{5}{\ell^5} \int_0^{\ell} z^2 \eta(z) dz \quad (10)$$

with units of $[\eta] = \text{W}^{-1} \cdot \text{m}^{-2}$, where $\tilde{\eta}z^2$ fits the normalized efficiency $\eta(z)$ in the least squares sense and ℓ is the actual length of the waveguide. Values of equivalent quantities are often given in literature in units of $\% \cdot \text{W}^{-1} \cdot \text{cm}^{-2}$.

Acknowledgments

The authors acknowledge the Fraunhofer Attract Grant SILIQUA No. 40-04866, the BMBF projects MEXSIQUO Grant No. 13N16967 and SINNER Grant No. 16KIS1792, and the Collaborative Research Center (CRC/SFB) 1375 NOA.

Conflict of Interest

The authors declare no conflict of interest.

Data Availability Statement

The data that support the findings of this study are available from the corresponding author upon reasonable request.

Keywords

Barium titanate, titanium dioxide, modal phase-matching, hybrid waveguide, nonlinear optics, integrated photonics

References

- [1] D. Sando, Y. Yang, C. Paillard, B. Dkhil, L. Bellaiche, V. Nagarajan, “Epitaxial Ferroelectric Oxide Thin Films for Optical Applications”, *Applied Physics Reviews* **2018**, *5*, 041108.
- [2] A. A. Demkov, A. B. Posadas, “Si-Integrated Ferroelectrics for Photonics and Optical Computing”, *MRS Bulletin* **2022**, *47*, 485.
- [3] K. Alexander, A. Benyamin, D. Black *et al.*, “A Manufacturable Platform for Photonic Quantum Computing”, *Nature* **2025**, *641*, 876.
- [4] A. Karvounis, F. Timp, V. V. Vogler-Neuling, R. Savo, R. Grange, “Barium Titanate Nanostructures and Thin Films for Photonics”, *Advanced Optical Materials* **2020**, *8*, 24.
- [5] A. Riedhauser, C. Möhl, J. Schading *et al.*, “Absorption loss and Kerr nonlinearity in barium titanate waveguides”, *APL Photonics* **2025**, *10*, 1.
- [6] A. Raju, D. Hungund, D. Krueger *et al.*, “High-Q Monolithic Ring Resonators in Low-Loss Barium Titanate on Silicon”, *Laser & Photonics Reviews* **2025**, *19*, 16.
- [7] G. I. Kim, J. Yim, G. Bahl, “Low loss monolithic barium titanate on insulator integrated photonics with intrinsic quality factor >1 million”, (Preprint) arXiv:2507.17150 submitted: July **2025**.
- [8] C. Xiong, W. H. P. Pernice, J. H. Ngai *et al.*, “Active Silicon Integrated Nanophotonics: Ferroelectric BaTiO₃ Devices”, *Nano Letters* **2014**, *14*, 1419.
- [9] S. Abel, F. Eltes, J. E. Ortmann *et al.*, “Large Pockels effect in micro- and nanostructured barium titanate integrated on silicon”, *Nature Materials* **2018**, *18*, 42.
- [10] Z. Dong, A. Raju, A. B. Posadas, M. Reynaud, A. A. Demkov, D. M. Wasserman, “Monolithic Barium Titanate Modulators on Silicon-on-Insulator Substrates”, *ACS Photonics* **2023**, *10*, 4367.
- [11] D. Chelladurai, M. Kohli, J. Winiger *et al.*, “Barium titanate and lithium niobate permittivity and Pockels coefficients from megahertz to sub-terahertz frequencies”, *Nature Materials* **2025**, *24*, 868.
- [12] C. Wang, C. Langrock, A. Marandi *et al.*, “Ultrahigh-efficiency wavelength conversion in nanophotonic periodically poled lithium niobate waveguides”, *Optica* **2018**, *5*, 1438.
- [13] M. Jankowski, C. Langrock, B. Desiatov *et al.*, “Ultrabroadband nonlinear optics in nanophotonic periodically poled lithium niobate waveguides”, *Optica* **2020**, *7*, 40.
- [14] J. Zhao, C. Ma, M. Rüsing, S. Mookherjea, “High Quality Entangled Photon Pair Generation in Periodically Poled Thin-Film Lithium Niobate Waveguides”, *Physical Review Letters* **2020**, *124*, 163603.
- [15] S. Choudhury, Y. L. Li, L. Q. Chen, Q. X. Jia, “Strain Effect on Coercive Field of Epitaxial Barium Titanate Thin Films”, *Applied Physics Letters* **2008**, *92*, 142907.
- [16] J. Paul, T. Nishimatsu, Y. Kawazoe, U. V. Waghmare, “Polarization Switching in Epitaxial Films of BaTiO₃: A Molecular Dynamics Study”, *Applied Physics Letters* **2008**, *93*, 242905.
- [17] A. S. Everhardt, S. Matzen, N. Domingo, G. Catalan, B. Noheda, “Ferroelectric Domain Structures in Low-Strain BaTiO₃”, *Advanced Electronic Materials* **2016**, *2*, 1500214.
- [18] Y. Jiang, E. Parsonnet, A. Qualls *et al.*, “Enabling Ultra-Low-Voltage Switching in BaTiO₃”, *Nature Materials* **2022**, *21*, 779.
- [19] W. Li, C. M. Landis, A. A. Demkov, “Evolution of Epitaxial BaTiO₃ on SrTiO₃-buffered Si: Phase Field Analysis”, *Journal of Applied Physics* **2022**, *132*, 213103.
- [20] S. Pal, L.-T. Hsu, H. Sun *et al.*, “Subsecond Optically Controlled Domain Switching in Freestanding Ferroelectric BaTiO₃ Membrane”, *Nature Communications* **2025**, *16*, 7940.
- [21] P. Aashna, H.-L. Lin, Y. Cao *et al.*, “Periodic Domain Inversion in Single Crystal Barium Titanate-on-Insulator Thin Film”, *Advanced Science* **2024**, *11*, 2406248.
- [22] I. Kim, A. A. Demkov, “Origin of Non-Absorptive Scattering Loss in Si-integrated Barium Titanate”, *Journal of Applied Physics* **2025**, *138*, 163110.
- [23] H. Du, X. Zhang, L. Wang, F. Chen, “Highly efficient, modal phase-matched second harmonic generation in a double-layered thin film lithium niobate waveguide”, *Optics Express* **2023**, *31*, 9713.
- [24] H. Du, X. Zhang, L. Wang, F. Chen, “Modal phase matching in z-cut dual-layered lithium niobate rib waveguide for second harmonic generation”, *Optics Express* **2025**, *33*, 23168.

[25] O. Hefti, J.-E. Tremblay, A. Volpini *et al.*, “Fabrication-tolerant modal phase matching for all-optical frequency conversion in layer-poled thin film lithium niobate waveguide”, *APL Photonics* **2025**, *10*, 10.

[26] R. Luo, Y. He, H. Liang, M. Li, Q. Lin, “Semi-Nonlinear Nanophotonic Waveguides for Highly Efficient Second-Harmonic Generation”, *Laser & Photonics Reviews* **2019**, *13*, 3.

[27] H. Honda, M. Okada, M. Uemukai, T. Tanikawa, R. Katayama, “Second harmonic generation in horizontally aligned AlN/SiN x hybrid waveguide for integrated wavelength converter”, *Applied Physics Express* **2025**.

[28] J. Wang, B. Wang, L. Fang *et al.*, “Second-Harmonic and Sum-Frequency Generation in Hybrid GaSe–SiN Waveguide”, *ACS Photonics* **2025**.

[29] J. Zhang, E. Cassan, D. Gao, X. Zhang, “Highly efficient phase-matched second harmonic generation using an asymmetric plasmonic slot waveguide configuration in hybrid polymer-silicon photonics”, *Optics Express* **2013**, *21*, 14876.

[30] C. C. Evans, C. Liu, J. Suntivich, “Low-loss titanium dioxide waveguides and resonators using a dielectric lift-off fabrication process”, *Optics Express* **2015**, *23*, 11160.

[31] P.-K. Hsu, Z.-W. Wang, M.-F. Chi, C.-C. Kuo, P.-H. Wang, “Development of high-quality TiO₂ photonics with E-gun evaporation”, *Optics Express* **2025**, *33*, 34510.

[32] T. Suhara, M. Fujimura, “Waveguide Nonlinear-Optic Devices”, Springer Berlin Heidelberg, **2003**.

[33] L. Mazet, S. M. Yang, S. V. Kalinin, S. Schamm-Chardon, C. Dubourdieu, “A Review of Molecular Beam Epitaxy of Ferroelectric BaTiO₃ Films on Si, Ge and GaAs Substrates and Their Applications”, *Science and Technology of Advanced Materials* **2015**, *16*, 036005.

[34] M. Reynaud, H. Huyan, C. Du *et al.*, “Si-Integrated BaTiO₃ for Electro-Optic Applications: Crystalline and Polarization Orientation Control”, *ACS Applied Electronic Materials* **2023**, *5*, 4605.

[35] T. Izuhara, I.-L. Gheorma, R. M. Osgood *et al.*, “Single-Crystal Barium Titanate Thin Films by Ion Slicing”, *Applied Physics Letters* **2003**, *82*, 616.

[36] Y.-B. Park, K. Diest, H. A. Atwater, “Single Crystalline BaTiO₃ Thin Films Synthesized Using Ion Implantation Induced Layer Transfer”, *Journal of Applied Physics* **2007**, *102*, 7.

[37] H. Esfandiar, F. Abtahi, T. G. Vrckovnik *et al.*, “Structural and Optical Properties of Crystal Ion Sliced BaTiO₃ Thin Films”, (Preprint) arXiv:2508.05874 submitted: Aug. **2025**.

[38] J. D. B. Bradley, C. C. Evans, J. T. Choy *et al.*, “Submicrometer-Wide Amorphous and Polycrystalline Anatase TiO₂ Waveguides for Microphotonic Devices”, *Optics Express* **2012**, *20*, 23821.

[39] M. Häyrinen, M. Roussey, V. Gandhi *et al.*, “Low-Loss Titanium Dioxide Strip Waveguides Fabricated by Atomic Layer Deposition”, *Journal of Lightwave Technology* **2014**, *32*, 208.

[40] I. Hegeman, M. Dijkstra, F. B. Segerink, W. Lee, S. M. Garcia-Blanco, “Development of Low-Loss TiO₂ Waveguides”, *Optics Express* **2020**, *28*, 5982.

[41] M. Fu, Y. Zheng, G. Li *et al.*, “High-Q titanium dioxide micro-ring resonators for integrated nonlinear photonics”, *Optics Express* **2023**, *28*, 39084.

[42] S. Abel, F. Eltes, J. E. Ortmann *et al.*, “Large Pockels Effect in Micro- and Nanostructured Barium Titanate Integrated on Silicon”, *Nature Materials* **2019**, *18*, 42.

[43] T. Jin, P. T. Lin, “Efficient Mid-Infrared Electro-Optical Waveguide Modulators Using Ferroelectric Barium Titanate”, *IEEE Journal of Selected Topics in Quantum Electronics* **2020**, *26*, 1.

[44] A. P. Aravind, H. Zhang, Y. Akimov *et al.*, “Second harmonic generation in gallium phosphide nano-waveguides”, *Optics Express* **2021**, *29*, 10307.

[45] L. Chang, Y. Li, N. Volet, L. Wang, J. Peters, J. Bowers, “Thin film wavelength converters for photonic integrated circuits”, *Optica* **2016**, *3*, 531.